Chapter

Low-Dimensional ZnO Nanostructures: Fabrication, Optical Properties, and Applications for Dye-Sensitized Solar Cells

Hsin-Ming Cheng and Shun-Wei Liu

Abstract

Zinc oxide nanostructure has a wide bandgap energy of 3.37 eV and a large exciton binding energy of 60 meV at room temperature. It is certainly a promising material for photonic devices in the ultraviolet to blue wavelength range. ZnO-related materials are also expected to construct the exciton as well as polariton lasers owing to their excitonic-stimulated emission and laser behavior under optically pumping can be obtained at ambient temperature. Because of the optical losses, including not only nonradiative recombination centers but also traps of excitons, the high quality of ZnO becomes even more imperative in the excitonic lasing processes. In the present chapter, ZnO nanowire structures via a low-pressure vapor-phase deposition and a simple solvothermal method will be presented. The one-dimensional ZnO nanowires could afford a direct conduction pathway to significantly enhance the overall efficiency of the dye-sensitized solar cells. Furthermore, this content will demonstrate how to employ the hierarchical structure of the ZnO nanoparticles, fabricated from sol-gel method, which could promote light scattering, thus, enhancing photon absorption and the overall solar conversion efficiency. The aim of this chapter is to present the correlation between the fundamental properties of ZnO nanostructures and their photovoltaics performances.

Keywords: zinc oxide, II–VI semiconductor, nanostructure, nanowire, nanoparticle, dye-sensitized solar cell

1. Introduction

Low-dimensional ZnO nanoparticles (NPs), quantum dots (QDs), and ZnO nanowires (NWs) have attracted much attention due to their good crystal quality, chemical stability, and unique optical properties. ZnO nanowire is also expected to play an important role because their manifold properties are interconnected as functional units in the fabrication of electronics, photonics, photocatalysts, and piezotronics with nanoscale dimensions. ZnO QDs and NPs are of great interest because of the three-dimensional confinement of carrier, and phonon leads not only continuous tuning of the optoelectronic properties but also improvement in

device performance. As a wide-bandgap semiconductor, ZnO has been reported as an alternative for dye-sensitized solar cells (DSCs) because ZnO offers a large direct bandgap which is close to TiO_2 and even higher electron mobility (155 $cm^2 V^{-1} s^{-1}$) for the high-quality thin film [1]. ZnO provides a promising alternative for improving the performance of the photoelectrode in DSCs because ZnO can be tailored to various nanostructures. In the present proposal, first, I will present the ZnO nanowire structures via a low-pressure vapor-phase deposition and a simple solvothermal method. The one-dimensional ZnO NWs could simultaneously afford a direct conduction pathway to significantly enhance the overall efficiency of the DSCs [2, 3]. Next, I also will demonstrate how to employ the hierarchical structure of the ZnO NPs, fabricated from sol-gel method, which would promote light scattering through the presence of secondary colloidal spheres, thus, enhancing photon absorption to improve the short-circuit current density and the overall light conversion efficiency.

2. ZnO nanostructures from solvothermal method

The process of the growth of the ZnO NWs is similar to Law et al. [2]. Arrays of ZnO NWs were synthesized on fluorine-doped tin oxide (FTO) substrates that were first cleaned thoroughly by sonication with acetone/ethanol and then coated with a thin film of ZnO QDs, 3–4 nm in diameter, by dip-coating in a 0.005 M $Zn(OAc)_2$-concentrated ethanol solution. The arrays of ZnO NWs were synthesized on seeded FTO substrates by immersing the seeded substrates in aqueous solutions containing 0.06 M zinc nitrate hydrate, 0.06 M hexamethylenetetramine (HMTA), and 7.5 mM polyethylenimine (PEI) at 95°C for 2.5–7.5 hours. **Figure 1** shows the tilted-view SEM images of the ZnO NWs on FTO layers and alumina-doped ZnO layers (AZO, 50~200 Ω per square), respectively. It seems that the aspect ratio (length against diameter) of nanowires can be increased when using PEI. The length and diameter of the PEI-absent ZnO NWs can be controlled in the range of about 300–500 nm and 300–400 nm, respectively. But, the length and diameter of the PEI-present ZnO NWs can be adjusted in the range of about 500–700 nm and 150–250 nm, respectively. The lengths of ZnO NWs are also prolonged while increasing the growth times. For example, the length and diameter of the ZnO NWs were in the range of about 2–3 μm and 250–350 nm, respectively, while the growth time is of 7.5 hours. Furthermore, the ZnO nanostructures with different morphology can be observed while using various substrates. The density and diameter of ZnO NWs seem to be influenced while using AZO substrates. The length and diameter of the ZnO NWs were in the range about 0.2–1.2 μm and 200–500 nm, respectively. By sputtering technique, it is reasonable to presume that the grain size of thick AZO films (200–300 nm) is bigger than dip-coating method, which caused the increase in the NW diameter and the good orientation as well. However, the fluctuation of diameter for ZnO NWs is huge while using AZO substrates, which could be related to the uniformity of AZO under layers.

Beyond the ZnO NWs, the impressive branched ZnO NWs have been fabricated successfully from solvothermal method [4]. First, the arrays of ZnO NWs were synthesized on seeded FTO substrates by immersing the seeded substrates in aqueous solutions containing 0.08 M zinc nitrate hydrate, 0.08 M HTMA, and 12 mM PEI at 95°C for 10 hours. Second, the ZnO NW substrate obtained from the first step were re-coated with seed layers of ZnO NPs by dip-coating in a 0.005 M $Zn(OAc)_2$ in ethanol. Then the branched NWs were grown by immersing the seeded ZnO NWs for a 5-hour duration in an aqueous solution containing 0.02 M zinc nitrate hydrate, 0.02 M HMTA, and 3 mM PEI at 95°C ambient. The final products were immediately rinsed with deionized water and baked in air at 450°C for 30 minutes to

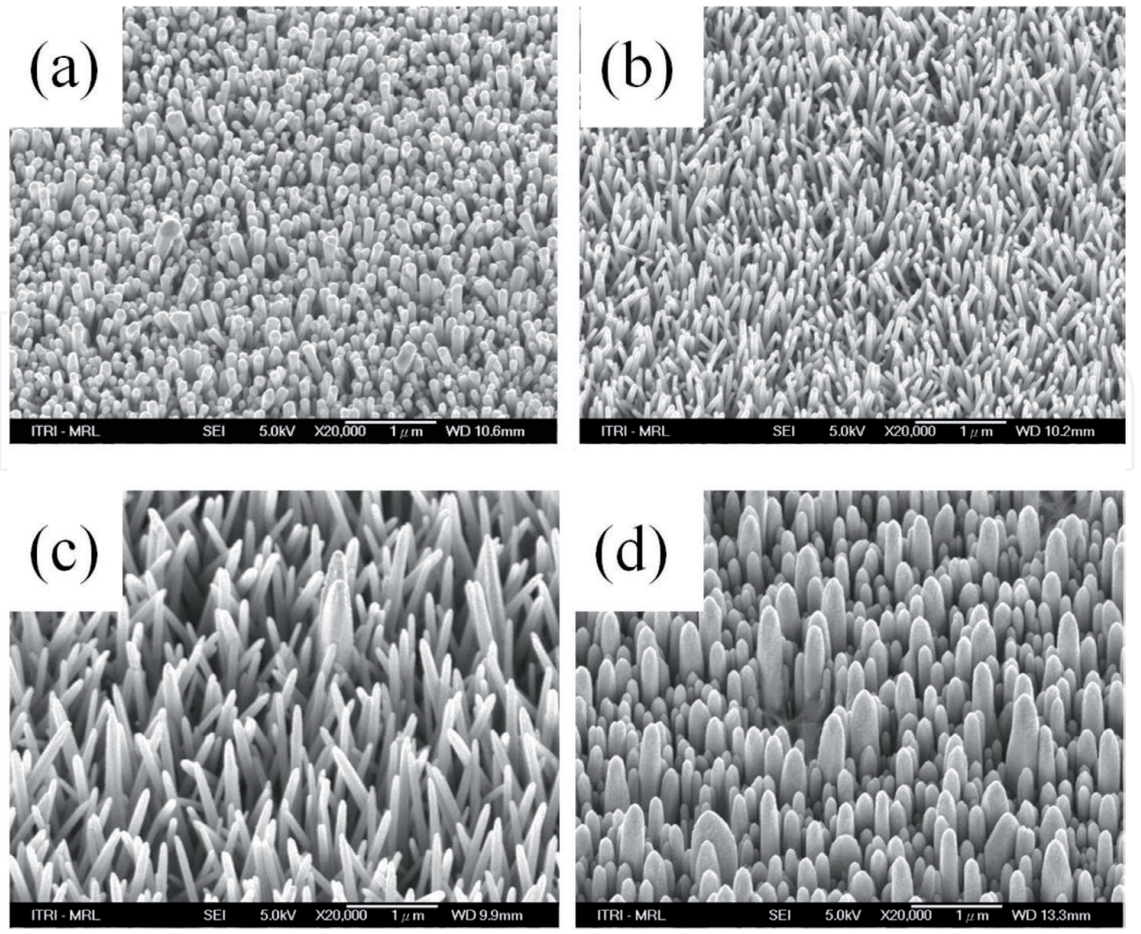

Figure 1.
The SEM images of the ZnO nanowires and nanorods with different growth conditions (a) FTO substrate, without PEI, grown 2.5 hours. (b) FTO substrate, with PEI, grown 2.5 hours. (c) FTO substrate, with PEI, grown 7.5 hours. (d) AZO substrate, with PEI and grown 7.5 hours.

remove any residual organics. The evolution of the ZnO NWs to the branched ZnO NWs is illustrated in **Figure 2a** and its corresponding FESEM images **Figure 2b–d**. By using a solvothermal method, the bare ZnO NWs with slight vertical off-alignment were grown perpendicularly on the FTO substrate, as shown in **Figure 2b**. Through the pre-coating process on the ZnO NWs, little ZnO crystallites with diameter 10–20 nm were formed on the backbone NWs, as shown in **Figure 2c**. After the second growth step, radial secondary ZnO branches emanated from the seeds, as shown in **Figure 2d**. The entire substrate in which the backbone nanowire has a density of about 7×10^8 cm^{-2} was covered with branched ZnO nanostructures. The backbone NWs have length and diameter in the range of 7–8 μm and 150–250 nm, respectively, whereas the secondary branches have length and diameter ranging from 100 to 300 nm and 20 to 50 nm, respectively. By the infiltration of moderately concentrated $Zn(OAc)_2$ solution into interstitial voids between backbone ZnO NWs, the branched ZnO NWs can successfully be fabricated.

Further structural characterizations of the branched ZnO NWs were performed by TEM. **Figure 3a** reveals the secondary ZnO branches which were grown on the side walls of nanowire backbone with different radial angles. The evidence confirmed the secondary ZnO branches were not the derivatives of ZnO NWs but definitely originated from the small crystallite ZnO seeds via the pre-coating process. Different from the other reports of comblike ZnO nanostructures which demonstrated the monolithically single-crystalline relationship between the branches and backbone nanowires [5, 6], in the present mechanism, the secondary ZnO branches were derived on the ZnO seeds in spite of the coordinate crystal relationship. The magnified intersection area of ZnO

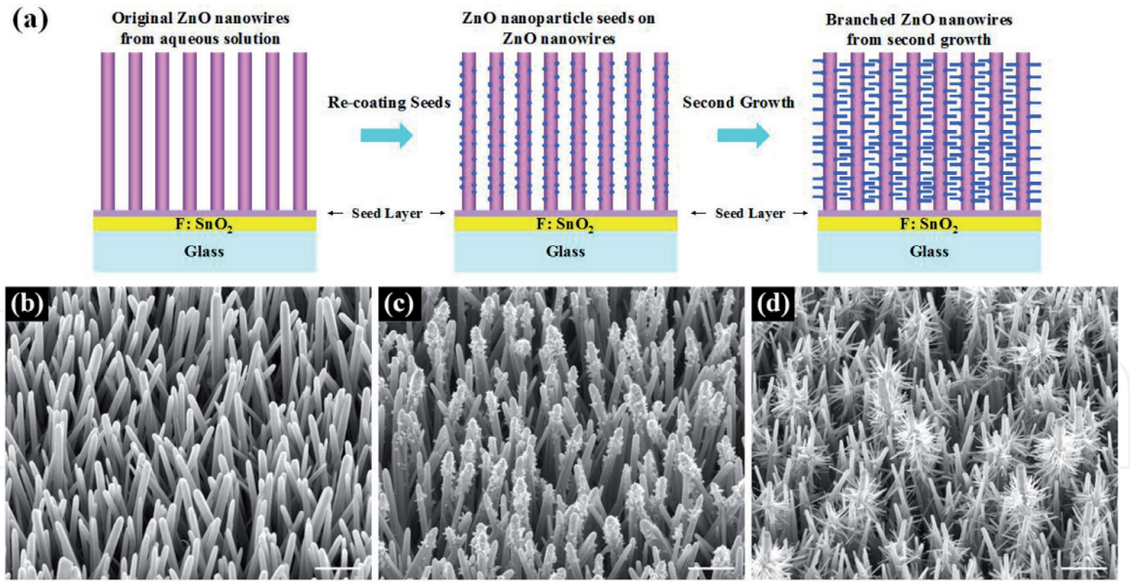

Figure 2.
(a) The schematic growth procedure from the original ZnO nanowires to the branched ZnO nanowires. (b) Before and (c) after re-coating a seed layer of the original ZnO nanowires obtained from a solvothermal method. (d) The branched ZnO nanowires after second growth. Scale bar, 1 μm [4].

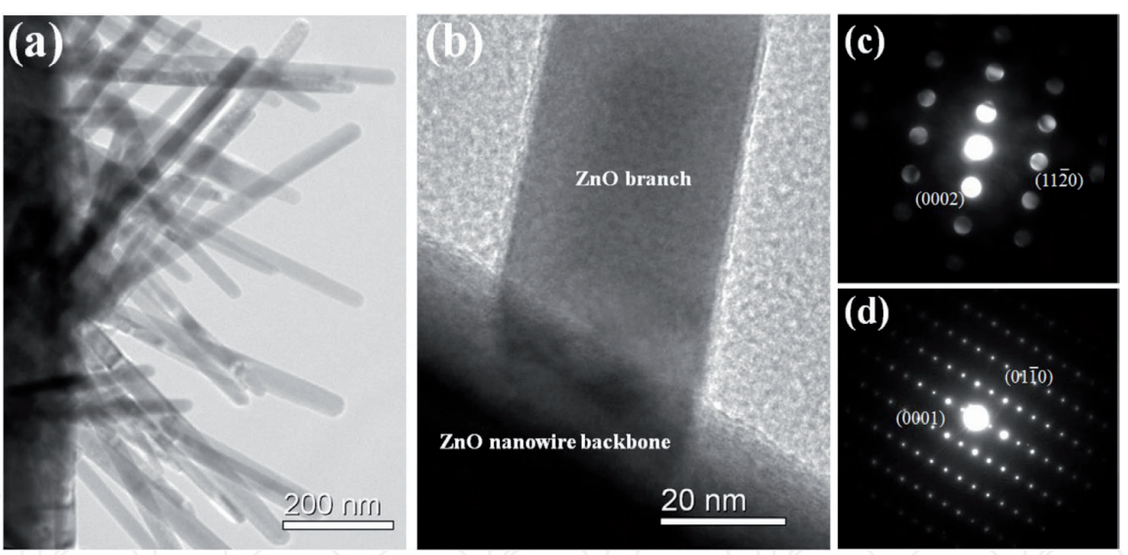

Figure 3.
(a) TEM image of a single-branched ZnO nanowire. (b) The magnified intersection area of ZnO branch and nanowire. (c and d) The corresponding nano-beam diffraction (NBD) and selected area electron diffraction (SAED) for the secondary ZnO branch and the ZnO nanowire backbone, respectively [4].

branch and nanowire was shown in **Figure 3b**. **Figure 3c**, **d** shows the corresponding nano-beam diffraction (NBD) of the secondary ZnO branch and selected area electron diffraction (SAED) of the ZnO nanowire backbone, respectively. The diffraction patterns confirmed each ZnO nanostructure was single-crystal wurtzite and preferentially oriented in the *c*-axis direction even though the two components of ZnO nanostructures were not fabricated simultaneously. The θ-2θ X-ray diffraction patterns of ZnO nanostructures, which corresponds to the hexagonal wurtzite crystallites with cell constants of a = 3.251 Å and c = 5.208 Å, were shown in **Figure 4a**. The strong {0001} diffraction family of ZnO once indicates that the nanowires are moderately oriented in the *c*-axis direction. It is presumed that all the precursors have been completely decomposed as no excess peaks can be detected. A Raman spectrum of the branched ZnO NWs, as shown in **Figure 4b**, which was taken from a 5 μm^2 spot size excited by a frequency-doubled

Yb:YAG laser (λ = 515 nm), obviously indicates the remarkable E_2 (low) and E_2 (high) modes of ZnO located at 98 and 438 cm^{-1}, respectively. The peak at 332 cm^{-1} is attributable to the second-order Raman scattering caused by the zone-boundary phonons 2-E_2(M) of ZnO. The weak and almost invisible signal near 581 cm^{-1} contributes to the superposition of A_1(LO) and E_1(LO). The substrate signal did not appear due to the penetrating limitation of the 515 nm laser. The good crystalline quality of ZnO nanostructures confirmed above ensures that the photoelectrode can provide good electronic conductivity without the defect trapping within the structures.

Secondary NPs herein were synthesized via sol-gel method [7]. The detailed synthetic process is similar to that described by Seelig et al. [8]. The structural evolution of products synthesized in various aging time using 10 ml of primary supernatant was shown in a series of SEM photographs as shown in **Figure 5**. The ZnO NPs were accumulated by white seeds from the beginning shown in **Figure 5a**.

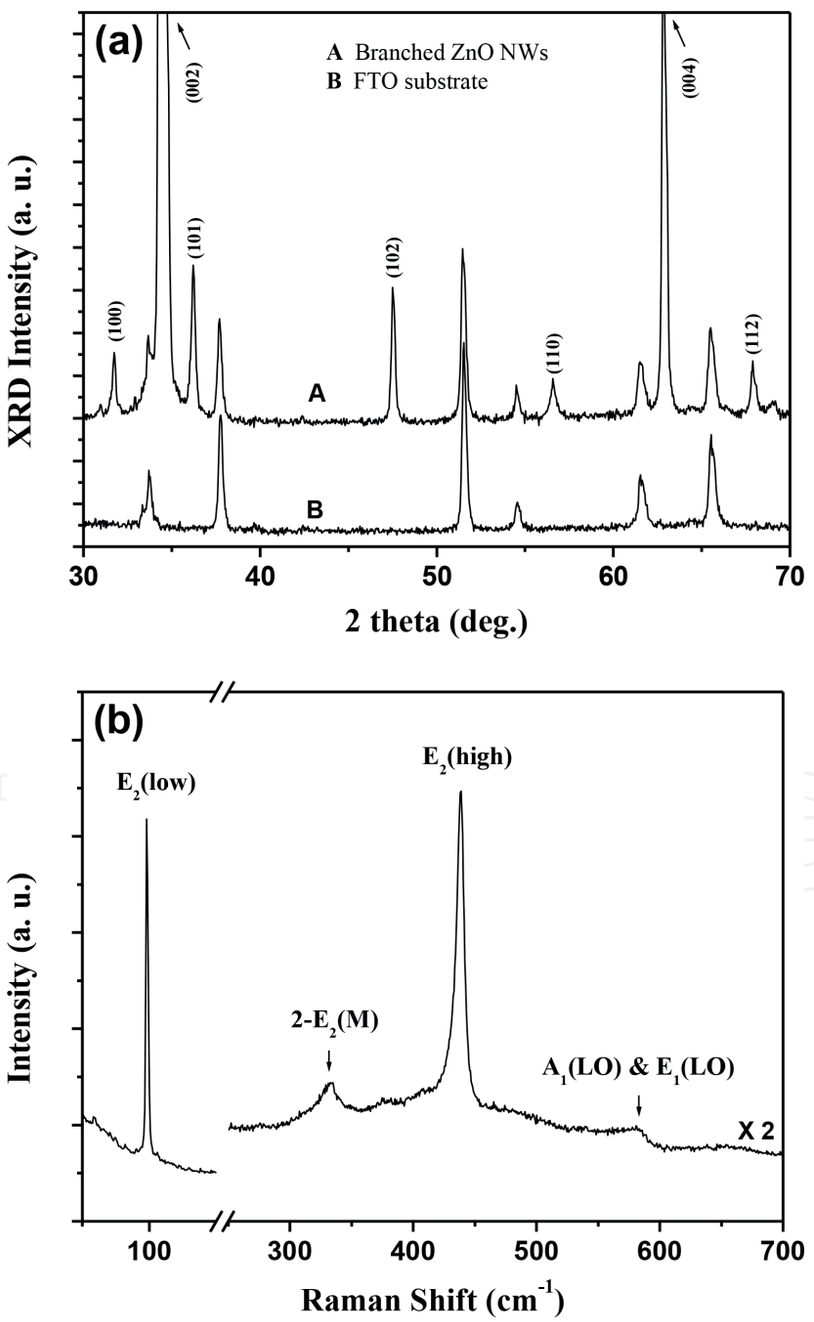

Figure 4.
(a) θ-2θ XRD profiles of A (the branched ZnO nanowires) and B (FTO substrate only). (b) Raman spectra of the branched ZnO nanowires, using a frequency-doubled Yb:YAG laser (λ= 515 nm) [4].

The zinc complexes were initially connected as a network (see **Figure 5b**) and condensed isotropic, eventually forming a hierarchical packing of colloidal particle, as shown in **Figure 5c**. The unidirectional aggregate phenomenon and formation mechanism in other metal oxide colloidal systems were presented by Serna et al. [9]. In at least 1-hour aging time, the monodispersed spherical ZnO NPs with an average particle size of ca. 185 nm could successfully be synthesized. The EDS spectra of the products with different aging time, as shown in **Figure 6**, reveal that they contain Zn, O, and C. As the aging time increases, the carbon ratio decreases, which means that the product requires complete aging time to remove the acetate ions.

Typical TEM micrographs of the ZnO NPs are shown in **Figure 7a–d**. A hierarchical packing of secondary ZnO NPs is formed in the condensation reaction of the sol-gel process, and the spherical shape of the ZnO NPs is recognized by the aggregation of many primary single crystals (also called subcrystals) ranging from 6 to 12 nm. It should be particularly noted here that when SAED is performed on several secondary ZnO NPs, the pattern exhibits a polycrystalline wurtzite structure of ZnO, as shown in the inset of **Figure 7a**. On the contrary, the pattern reveals the single-crystal-like diffraction, as shown in the inset of **Figure 7b**, while restricting the SAED area within only one ZnO NP. Obviously, the secondary ZnO NPs are polycrystals consisting of much smaller subcrystals of the same crystal orientation. More evidence can be demonstrated in the high-resolution TEM (HRTEM) image from both the center and the edge of the ZnO NPs in **Figure 7b**, **c**, respectively. In most cases, van der Waals interacts as a driving force for self-assembly between surface molecules of nanocrystallites, which can then assemble colloidal nanocrystals to form solids. If the size distribution of the nanocrystals is sufficiently small, an ordered array (also known as a superlattice), a quantum dot, or an artificial solid is formed by self-assembly [11, 12]. Therefore, the growth of the above secondary ZnO nanoparticles could be carried out in substantially the same way, with some discontinuities between the subunits, and each subcrystal is a subunit of the secondary ZnO NPs. Sugimoto et al. also reported similar self-assembly structures in α-Fe_2O_3 particles [13, 14]. The reason for the discontinuity of the internal structure is explained by the strong adsorption of ions used in the

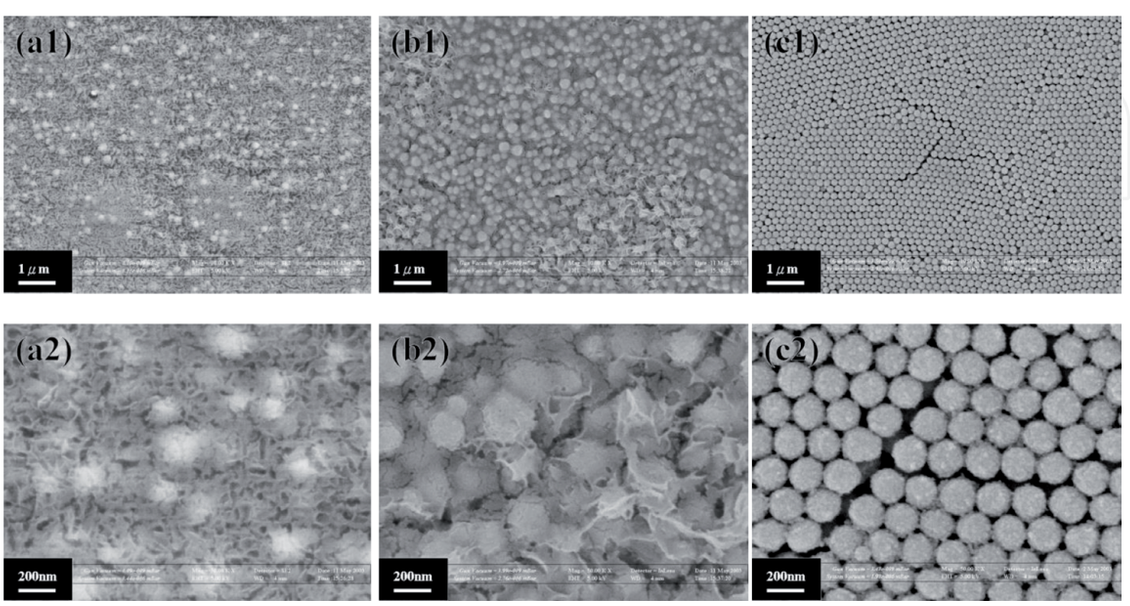

Figure 5.
Large and local scale of scanning electron micrographs of various aging time products synthesized using 10 ml of primary supernatant. The aging times are (a) 15 minutes, (b) 30 minutes, and (c) 60 minutes, respectively [7].

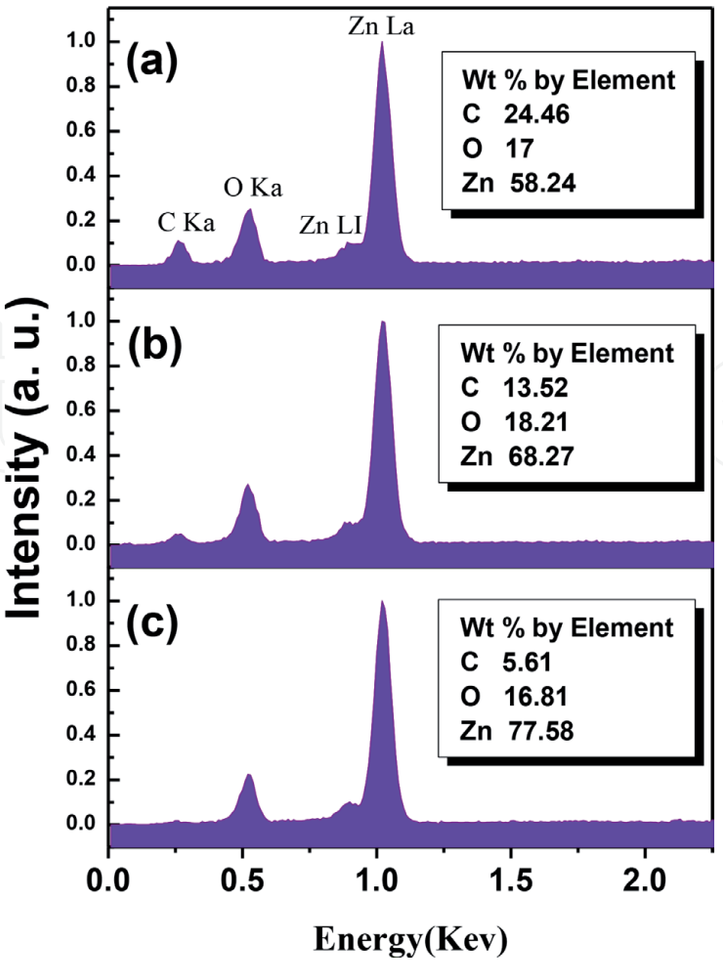

Figure 6.
Composition-variation analysis by energy dispersive x-ray spectra (EDS) of different aging time products as (a) 15 minutes, (b) 30 minutes, and (c) 60 minutes [7].

reaction to prevent the fusion between the surface grains [15–17]. Although there is no existence of ions throughout the whole process in this present work. It is suspected that due to the blockage of DEG, the solvent appears as a microemulsion system, resulting in the separate growth of the ZnO subcrystals alone and eventually assembled under the driving force of the van der Waals interaction to form secondary NPs. As shown in **Figure 7d**, the subcrystal is a perfect crystal and exhibits a facet for which the evidence is specifically described in the HRTEM image of the edge of ZnO NPs. Thus, the subcrystals slowly self-assemble by sintering and belonging to the same defined orientation as the adjacent subcrystals.

It is interesting that the evolutions of morphology of ZnO NPs show the subcrystals significantly fused with the neighbor crystals during the heating process. **Figure 8a–c** displays the SEM images of as-grown ZnO NPs and the samples after post-annealing at 350 and 500°C in air ambient for 1 hour, respectively. The grain growth was also investigated from the XRD profiles (not shown here) and Scherrer formula, as the crystalline sizes were estimated to be approximately 9, 14, and 20 nm for as-grown, 350°C-annealed, and 500°C-annealed samples, respectively. Raman spectroscopy was performed to investigate the vibrational properties of the secondary ZnO NPs before and after being heat treated. For the wurtzite structure of ZnO, which belongs to the space group $C_{6\upsilon}^4$ ($P6_3mc$), one primitive cell includes two formula units, with all of the atoms occupying 2*b* sites of symmetry $C_{3\nu}$. **Figure 9** shows a normal Raman spectra by a frequency-doubled Yb:YAG laser (λ = 515 nm). The remarkable feature at 520 cm^{-1} is due to the TO phonon mode from the Si substrate, while the peak at 437 cm^{-1} corresponds to E_2(high) of

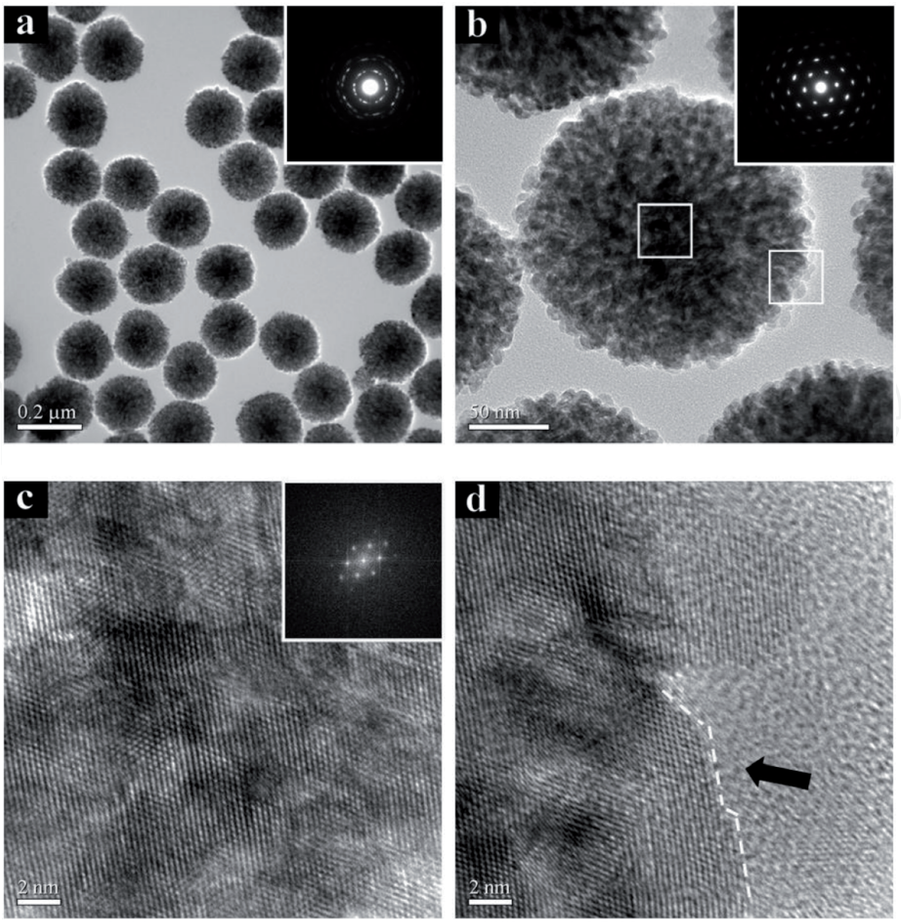

Figure 7.
TEM images of secondary ZnO NPs recognized of crystalline subcrystals. (a) A typical low-magnification TEM image and SAED pattern of several uniform ZnO NPs. (b) High-magnification TEM image of one individual ZnO NP and its corresponding single crystal-like SAED spots. (c and d) High-resolution TEM images of central area and boundary part of one individual ZnO NP, respectively. Inset of (c) corresponding fast Fourier transform image [10].

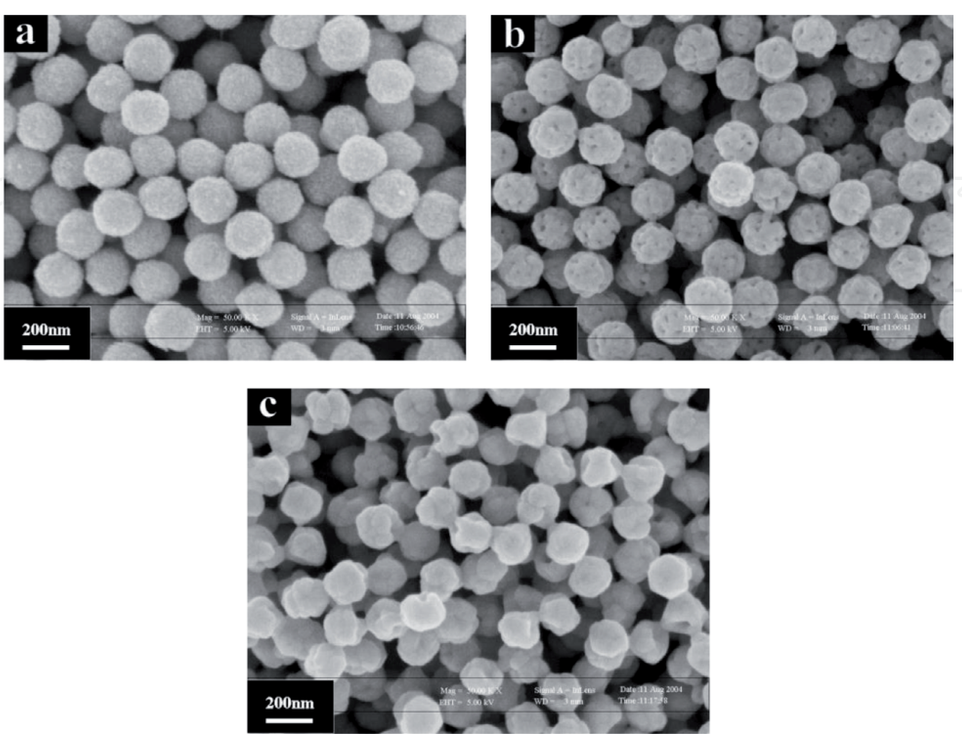

Figure 8.
SEM micrographs of (a) as-grown, (b) 350°C annealing for 1 hour, and (c) 500°C annealing for 1 hour secondary ZnO NPs, respectively [10].

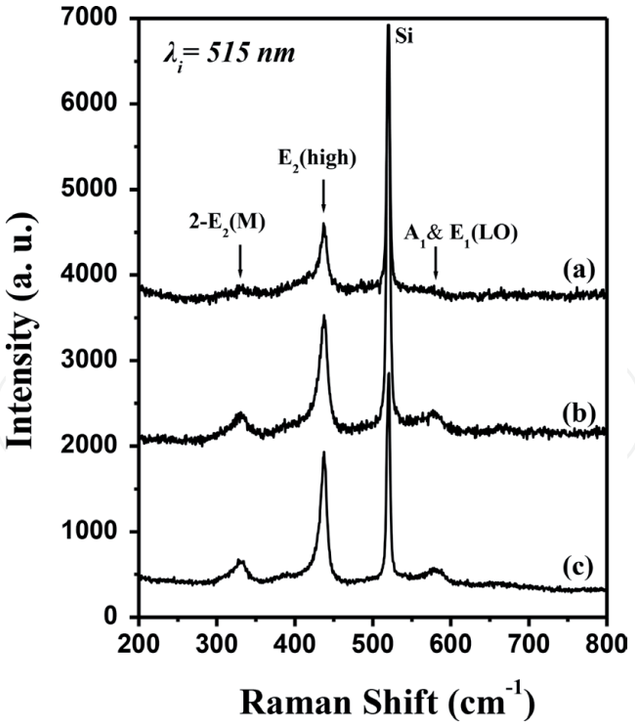

Figure 9.
Normal Raman spectra of (a) as-grown, (b) 350°C annealing for 1 hour, and (c) 500°C annealing for 1 hour secondary ZnO NPs, using a frequency-doubled Yb:YAG laser (=515 nm) [10].

ZnO. The peak at 331 cm^{-1} can be assigned to the second-order Raman scattering arising from zone-boundary phonons 2-E_2 (M) of ZnO. No significant change of Raman spectra and intense E_2 (high) peak for the 350°C-annealed and 500°C-annealed samples means good crystallinity. The full width at half-maximum (FWHM) of Raman E_2(high) peak decreases (from 14 to 11 cm^{-1}) as the crystal size increases as anneal temperature from 350˚C to 500˚C, which is consistent with the XRD results. Another imperceptible broadened peak around 580 cm^{-1} is contributed to the superposition of A_1(LO) and E_1 (LO). The lattice behavior of A_1 (LO) and E_1 (LO) modes is associated with the existence of some nonstoichiometric defects while heat treatment, such as oxygen vacancy, interstitial zinc, or their complexes [18–20] those are produced due to the unfavorable process environment.

In principle the electron-phonon interaction could be investigated by utilizing resonant Raman scattering (RRS) experiments. The excitation photon energy resonates with the transition energy above the electron bands of wurtzite ZnO, so that a He-Cd laser (= 325 nm) was used as the excitation source for RRS. The A_1 (LO) and E_1 (LO) modes would dominate as their polar symmetric and exhibit different frequencies from the TO modes as well. As shown in **Figure 10**, intense multiphonon scatterings of the secondary ZnO NPs before and after heat treatment were observed, where the major peaks were observed as a result from the polar symmetry modes A_1 (LO) and E_1(LO) and their overtones. For the superposition of LO phonon mode, the Zn atoms and the O atoms have the same vibration direction as the adjacent lattice, respectively [21], while the weak peak, which is contributed to the E_2(high) mode around 437 cm^{-1}, is almost imperceptible. Multiphonon scattering processes also have been previously reported for single-crystalline bulk ZnO [22], ZnO films [23], ZnO-opal structures [24], and ZnO NWs [25, 26] but rarely mentioned for ZnO NPs.

It is worth noting that the intensity of the first-order Raman mode and its overtone are enhanced in the grown ZnO NP compared to the annealed sample. The reason can be explained by the total Raman cross section for an n-phonon process written as [27, 28]

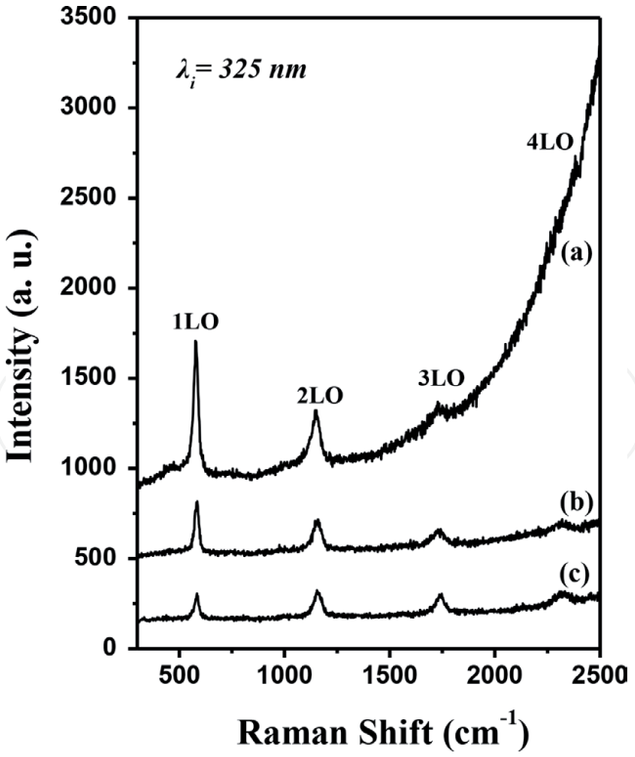

Figure 10.
Resonant Raman scatterings (RRS) of (a) as-grown, (b) 350°C annealing for 1 hour, and (c) 500°C annealing for 1 hour secondary ZnO NPs, using a He-Cd laser (= 325 nm) [10].

$$\sigma_n = \int \sigma_n^R(\omega) f(R) dR, \tag{1}$$

$$\sigma_n^R(\omega) = \mu^4 \left| \sum_{m=0}^{\infty} \frac{\langle n|m\rangle\langle m|0\rangle}{E_0 + n\hbar\omega_{LO} - \hbar\omega + i\hbar\Gamma} \right|^2 \times \exp\left(-\frac{i\hbar\omega_{LO}}{k_B T}\right), \tag{2}$$

where μ is the electronic dipole transition moment; E_0 is the size-dependent energy of the electronic transition; $\hbar\omega$ and $\hbar\omega_{LO}$ are the energies of the excitation photon and the LO phonon, respectively; m denotes the intermediate vibrational level in the excited state; Γ is the homogeneous linewidth; k_B is Boltzmann's constant; T is the temperature; and the bracket indicates the overlap integral between the ground and excited state wave functions. Consequently, the RRS intensity can be enhanced as the denominator in Raman scattering cross section tending to zero, while the electronic state in the material is close to the incident or scattered photons. Similar results have been previously reported for CdS and ZnO, using various laser wavelengths [29]. Due to the quantum confinement effect of the subcrystal size relative to the exciton radius, the bandgap of the as-grown ZnO NPs would tend to approach the excitation laser energy. Evidence of quantum confinement can be found by the intensive tail of the blue-shifted photoluminescence (PL) signal of the as-grown ZnO NPs, or it can be found in the RRS spectrum rather than in the normal RS spectrum due to their red-shifted, broadening and asymmetry.

Due to the infinite correlation length, the phonon eigenstate in an ideal crystal is a plane wave; therefore, the $K = 0$ momentum selection rule of the first-order Raman spectrum can be satisfied. When the crystalline is reduced to nanometer scale, the momentum selection rule will be relaxed. This allows the phonon with wave vector $|k| = |k'| \pm 2\pi/L$ to participate in the first-order Raman scattering, where k' is the wave vector of the incident light and L is the size of the crystal.

The phonon scattering is not limited to the center of the Brillouin region. In order to observe the displacement, broadening, and asymmetry of the first-order optical phonon, the phonon dispersion near the center of the region must also be considered. Alim et al. [30, 31] have shown that the large red-shift in the resonant Raman spectrum from 20 nm ZnO NPs is most likely due to local heating by UV laser excitation. In this study, since the as-grown secondary ZnO NPs contain more air gaps than the annealed NPs, an unfavorable heat dissipation may be the other possibility of causing higher temperatures and greater phonon red-shift. For the clarity, detailed numerical analysis of the ZnO NPs of this experiment is clearly listed in **Table 1**. It was found that the ratio between the second-order and first-order Raman scattering cross sections increased from 0.38 to 2.05, while the ZnO crystallite size increased from nanoparticle to bulk. In the Franck-Condon approximation, the coupling strength of the [32, 33] exciton transition to the LO phonon can be expressed by the Huang-Rhys parameter *S*. The cross section of the RRS depends on the particle size, temperature, and excitation wavelength. Scamarico et al. [34] proposed that due to the strong energy dependence of the Raman scattering cross section, it is necessary to maintain resonance conditions in order to make meaningful comparisons with spectra of nanocrystals of different sizes to maintain different electronic transitions. It is important to purposefully use the same experimental conditions, such as laser power, wavelength, spot size, etc. for each sample. In this study, I emphasize that the tendency here is the increasing electron-phonon interaction with increasing nanocrystal size. It is generally accepted that the electron-phonon coupling is determined by the deformation potential and the Fröhlich potential. TO Raman scattering cross section is mainly determined by the deformation potential that involves the short-range interaction between the lattice displacement and the electrons [35, 36]. On the other hand, the LO Raman scattering cross section includes contributions not only the Fröhlich potential that involves the long-range interaction generated by the macroscopic electric field associated with the LO phonons but also the deformation potential. The intensity of TO phonons in ZnO NPs was found to be almost insensitive, while the intensity of LO phonons was greatly enhanced under resonance conditions. This study shows that electron-LO-phonon coupling is related to the Fröhlich interaction as the size of the nanocrystals decreases. Although the complex origin is not clear, the results of this study are very similar to those of other low-dimensional ZnO nanostructures, such as ZnO-based quantum wells [37] and ZnO NWs [38].

	As-grown[a]	**350°C**[a]	**500°C**[a]	**Bulk**[b]
Grain size (nm)	9	14	20	>1000
1LO (cm^{-1}) (FWHM)	578 (27.2)	582 (24.2)	584 (23.9)	585 (N/A)
2LO (cm^{-1}) (FWHM)	1149 (54.7)	1154 (49.3)	1158 (47.3)	1165 (N/A)
I_{2LO}/I_{1LO}	0.38	0.59	1.07	2.05

[a]*This content*
[b]*From Ref. [22] (used the same He-Cd laser, λ= 325 nm, as the excitation source for RRS)*

Table 1.
Wave number, broadening, and the ratio of n-LO phonons found in RRS spectra. The assignments of bulk ZnO are also listed as a Ref. [10].

3. ZnO nanostructures for dye-sensitized solar cells

DSCs were prepared by immersing the area-defined ZnO NW specimens into a solution of 0.5 mM cis-bis(isothiocyanato)bis(2,2′-bipyridyl-4,4′-dicarboxylato)-ruthenium(II)bis-tetrabutylammonium (N719, Solaronix) in acetonitrile/*tert*-butanol (1:1) for 20 minutes. After rinsing with acetonitrile and natural drying, the sensitized electrodes were sandwiched together with thermally platinized FTO counter electrodes separated by 25-μm-thick hot-melt spacers (Surlyn, Dupont). The electrolyte solution (0.1 M LiI, 0.5 M 1,2-dimethyl-3-propylimidazolium iodide, 0.03 M I_2, and 0.5 M *tert*-butylpyridine in acetonitrile) was filled into the internal space.

The comparison of photocurrent-voltage (J-V) characteristics for solar cells which was constructed using the bare ZnO NWs and the branched ZnO NWs with AM 1.5 illumination at 100 mW/cm^2 from a xenon lamp was shown in **Figure 11**. The overall light conversion efficiency and short-circuit current density (J_{sc}) of the branched ZnO nanowire DSCs were 1.51% and 4.27 mA/cm^2, respectively, which are almost twice higher than that of the bare ZnO NWs. Increased photon absorption is associated with an increase in internal surface area, resulting in enough dye loading as a major factor in the increase in short-circuit current density. Although the density of ZnO structures exhibits the insignificancy compared with some previous studies, the shortage can be complemented via the extra branches. The values of fill factor (*FF*) for ZnO DSCs are generally low (~0.5) which is attributed to recombination between photoexcited carriers and triiodide ions in the photoanodes and electrolyte, respectively. No obvious difference of the shunt resistance $R_{sh} = (dV/dI)_{V=0}$ from the J-V curves under illumination revealed almost the same interfacial recombination; however, the series resistance $R_s = (dV/dI)_{I=0}$ for branched ZnO nanowire DSCs (25.64 Ωcm^2) was significantly lower than the bare ZnO nanowire ones (46.13 Ωcm^2).

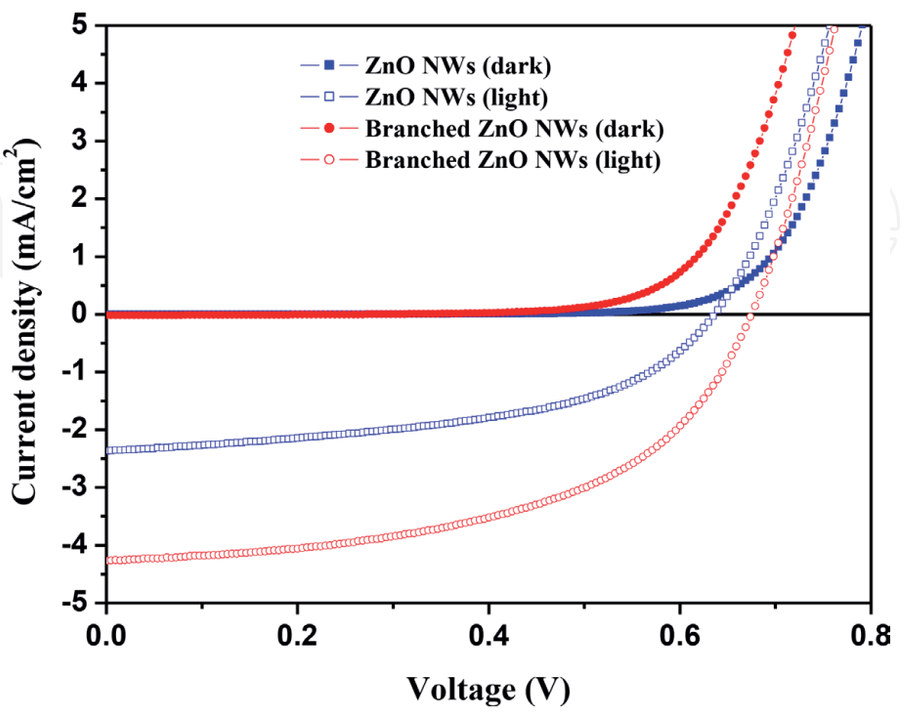

Figure 11.
Current density against voltage (J-V) characteristics of the bare ZnO nanowires and the branched ZnO nanowire DSCs [4].

Some interior parameters of DSCs can be analyzed by the impedance data of the Nyquist plots. The modified equivalent circuit of nanowire DSCs was suggested by Wu et al. [39, 40]. **Figure 12** shows the impedance data for bare and branched ZnO nanowire DSCs performed by applying a 10 mV ac signal over the frequency range of 10^{-2}–10^{5} Hz under illumination at the applied bias of V_{oc}. r_w and r_k are the transport resistance of the electrons in the ZnO electrode and the charge-transfer resistance of the charge recombination between electrons in the ZnO electrode and I_3^- in the electrolyte, respectively. The thickness L_F of all anodes are about 8 μm; $C_\mu = (c_\mu L_F)$ is the chemical capacitance of the ZnO electrode; *Rs* is a summary resistance for the transport resistance of FTO and other resistances out of the cell; Z_N is the impedance of diffusion of I_3^- in the electrolyte; C_{Pt} and R_{Pt} are the interfacial capacitance and the charge-transfer resistance at the counter electrode (platinized FTO glass)/electrolyte interface, respectively; C_{FTO} and R_{FTO} are the interfacial

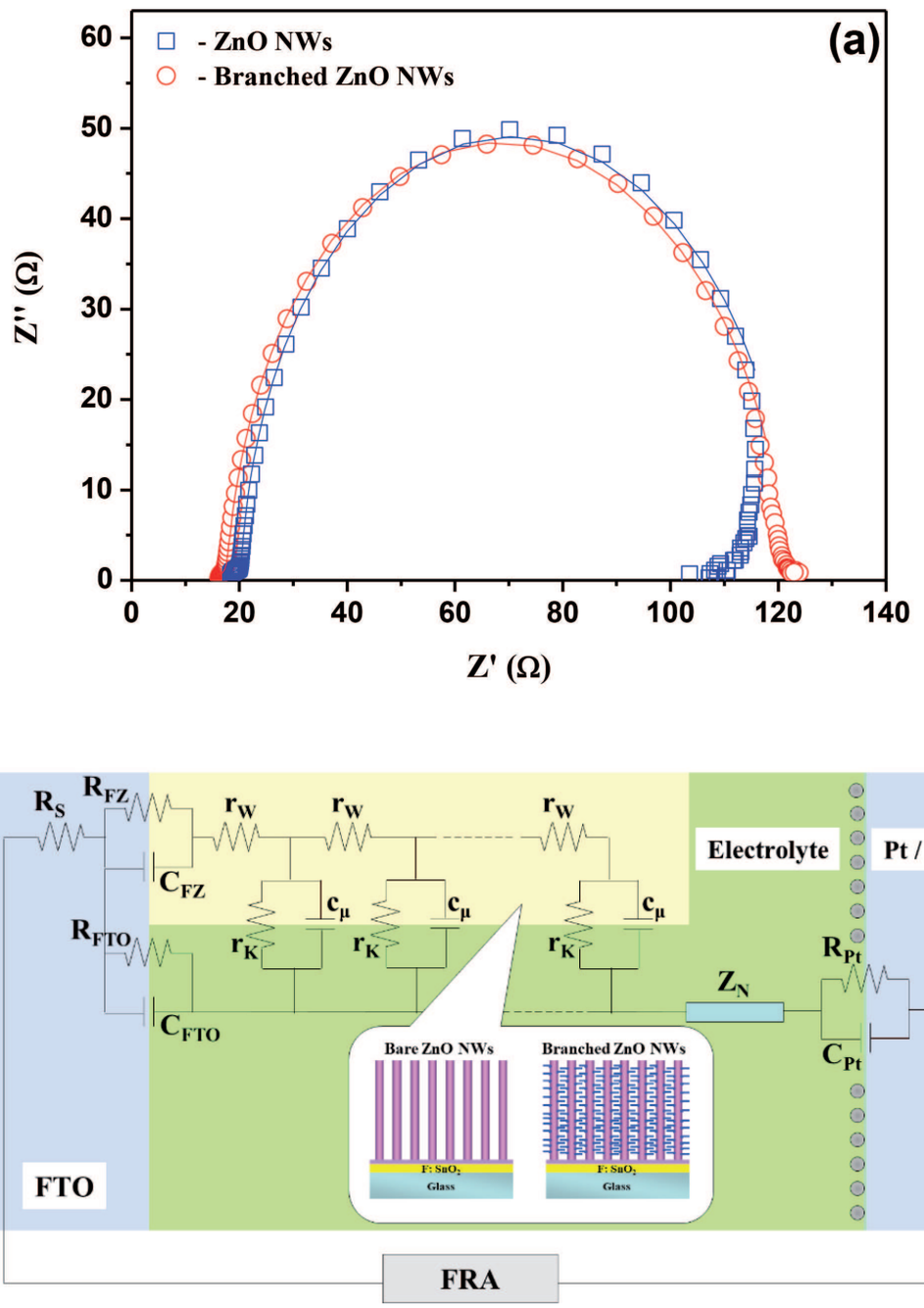

Figure 12.
Nyquist plots of the bare ZnO nanowires and the branched ZnO nanowire DSCs. The solid lines are the fitting results based on the equivalent circuit model (modified from ref. [41] as shown in the inset) [4].

capacitance and the charge-transfer resistance at the exposed FTO/electrolyte interface, respectively; C_{FZ} and R_{FZ} are the capacitance and resistance at the FTO/ZnO contact, respectively.

The specific equivalent circuit might be more complicated while operating the DSCs. Mora-Seró et al. have reported the conductivity modulation of the electrolyte-induced negative capacitance which comes from by injected electrons from the photoelectrode while providing high forward bias with low frequency [42]. In order to avoid the unnecessary interference from the inductor, the low-frequency part of impedance data was currently ignored. The fitted results of the first-order reaction rate constant for the loss of electrons(k_{eff}), the electron lifetime ($\tau = 1/k_{eff}$), the electron transport resistance ($R_w = r_w L_F$), and the charge-transfer resistance related to recombination of an electron at the ZnO/electrolyte interface ($R_k = r_k/L_F$) were listed in **Table 2**. R_k and R_w are quite similar for both DSCs which meant the same crystallinity and interfacial recombination for either bare ZnO NWs or branched ZnO nanostructures. k_{eff} in the branched ZnO nanowire DSCs was smaller than the bare nanowire ones to cause the smaller effective diffusion length [43] ($D_{eff} = (R_k/R_w)L_F^2 k_{eff}$) in branched ZnO nanowire DSCs. But the electron lifetime ($\tau_{eff} = 1/k_{eff}$) was prolonged by the additional transport distance of branched ZnO nanowire DSCs.

The current density of a DSC is determined by the amount of photogenerated carriers, the electron injection efficiency from the dye molecules to the semiconductor, and the recombination rate between the injected electrons and the oxidative dye or redox species in the electrolyte. The initial amount of photogenerated carriers may have a significant effect on the light-harvesting ability of photoanodes of different structures. **Figure 13** displays the comparison of incident monochromatic photon to current conversion efficiency (IPCE). The peaks at approximately 400 nm were due to direct light harvesting by ZnO semiconductor. The photogenerated electrons diffused through ZnO and the holes in the valence band were replenished directly by charge transfer from the I_3^-/I^-electrolyte [44]. The maximum peak at approximately 525 nm is contributed by the dye absorption, corresponding to the visible $t_2 \rightarrow \pi^*$ metal-to-ligand charge transfer (MLCT). The IPCE obtained for the branched ZnO nanowire DSCs was almost 1.5 times that of the bare ones. This improvement is primarily due to sufficient dye loading of the branched ZnO NWs, which increases the internal surface area within the photoelectrode. From the dye loading measurement, as shown in **Figure 14**, the concentration of dye in the branched ZnO nanowire electrode was found to be 2.9×10^{-9} mol/cm^{-2} as measured from dye-desorption experiments, which is almost 40% higher than the obtained value of 2.1×10^{-9} mol/cm^{-2} for the bare ZnO nanowire electrode.

It is worth noting that even though the current density and energy conversion efficiency of branched ZnO DSCs is twice that of bare ZnO ones, the dye loading

ZnO DSCs	J_{sc} (mA/cm^2)	V_{oc} (V)	*FF*	η (%)	k_{eff} (s^{-1})	τ_{eff} (s)	R_k (Ω)	R_w (Ω)	D_{eff} (cm^2/s)
Bare nanowires	2.37	0.636	0.498	0.75	38.31	0.026	92.12	3.63	6.23×10^{-4}
Branched nanowires	4.27	0.675	0.522	1.51	26.31	0.038	86.85	3.36	4.35×10^{-4}

Table 2.
Performances and electron transport properties of the bare ZnO nanowire and the branched ZnO nanowire DSCs determined by photocurrent density-voltage (J-V) characteristics and electrochemical impedance spectroscopy (EIS) analysis [4].

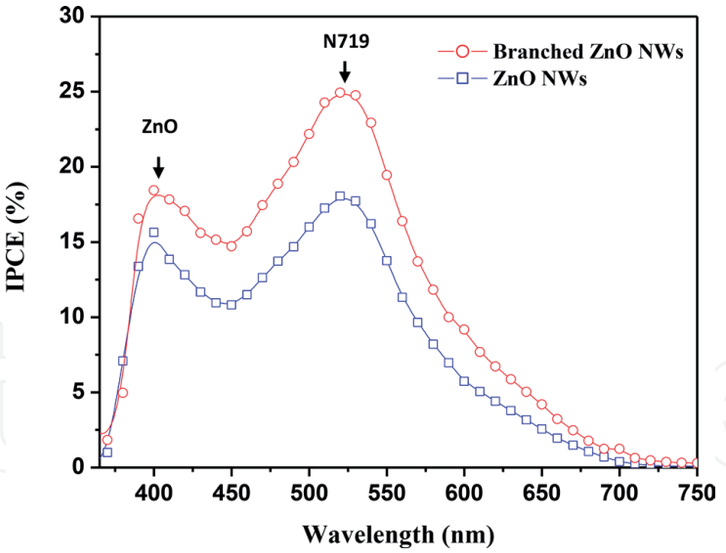

Figure 13.
The incident monochromatic photon to current conversion efficiency (IPCE) of the bare ZnO nanowire and the branched ZnO nanowire DSCs [4].

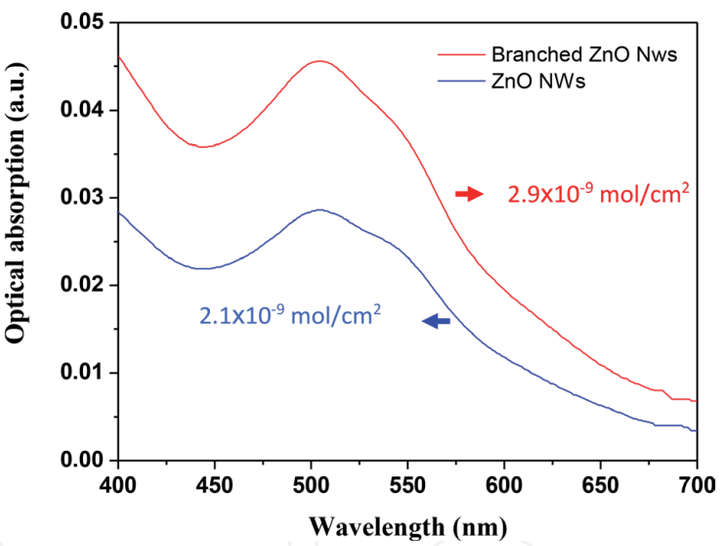

Figure 14.
Optical absorption of dye detached from the bare ZnO nanowire and the branched ZnO nanowire substrates and dissolved in 0.1 M NaOH solution [4].

of branched ZnO DSCs is not twice that of bare ZnO ones. The differences may be that the internal surface of the bare ZnO NWs is insufficient and the excess dye results in the formation of Zn^{2+}/dye complexes rather than an effective chemical bond between the ZnO and dye molecules. To avoid the excessive reaction, Chou et al. [45] reported the shorter immersion time for deficient chemical stability ZnO electrode as compared with TiO_2 electrode. Therefore, the excess immersion time of the insufficient internal surface of bare ZnO NWs cannot achieve more dye loading but seriously deteriorates the performance of the DSCs. Although the secondary branches have a nonuniform distribution due to the simple dip-coating process, the branches emitted from a portion of the ZnO NWs could still provide a greater effective surface area for dye adsorption than the bare NWs. The dc or radio frequency (RF) magnetron sputtering or atomic layer deposition (ALD) is suggested to apply great benefit to the pre-coating processes for the optimization of the filling factor of the ZnO NWs. Further improvement of light harvesting, current density, and

overwhelm energy conversion efficiency could be implemented through adjusting denser and longer branches to fill the interstitial voids between backbone NWs.

Hierarchically packed ZnO NPs were formed in the condensation reactions of the sol-gel process that was mentioned previously. The diameter of the ZnO NPs in the range of 160–680 nm was used as shown in **Figure 15a**. **Figure 15b** shows the spherical-shaped secondary ZnO NPs with the diameter of 680 nm. The similar ZnO architectures have been elucidated as the random lasing applications in which the cavities were formed by multiple scattering (UV range) between ZnO primary particles [47]. The laser action comes from an efficient amplification along the closed-loop light-scattering path within a secondary ZnO nanoparticle. Recently, Cao et al. have demonstrated that the aggregation of ZnO nanocrystallites performs an effective scheme to generate multiple light scattering (sunlight range) within the photoelectrode film of DSCs without using any other scattering layers [48, 49], as shown in **Figure 15c**. With utilization of ruthenium complex *cis*-$[RuL_2(NCS)_2]$ (L = 4,4′-dicarboxy-2,2′-bipyridine), N3 dye, Cao achieved the maximum energy conversion efficiency of 5.4%.

In this present research, a broad size distribution of secondary ZnO NPs with mean radius of 360 nm, as shown in **Figure 16a**, is controlled to provide the wide-range absorption of visible sunlight within the preferable packing of the ZnO photoelectrode. The hierarchical ZnO photoelectrode provides the multiple scattering of light, and therefore the light-traveling distance can be significantly prolonged. Furthermore, the primary ZnO nanocrystallites could supply internal surface area to allow enough adsorption of dye molecules. From the optical absorption spectra, the intrinsic exciton absorption (direct transition of energy bandgap of ZnO) could

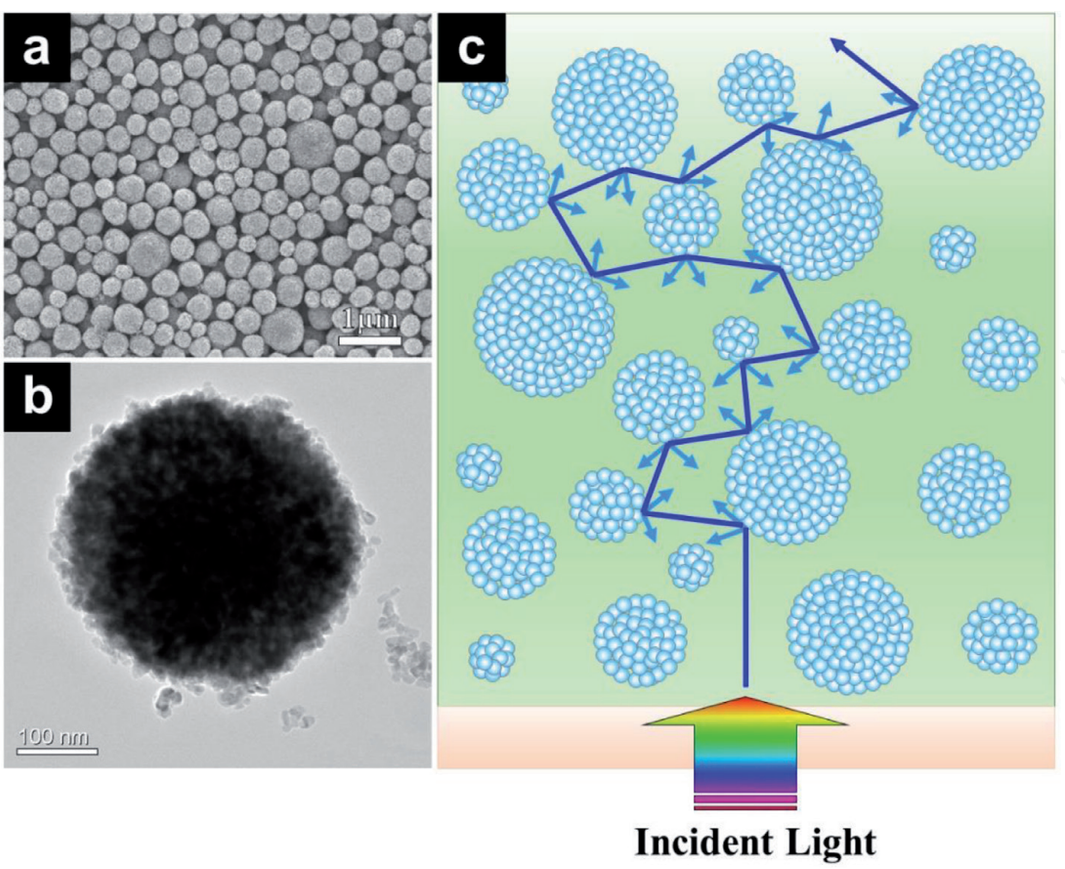

Figure 15.
(a, b) The FESEM and TEM images for the self-assembled ZnO secondary nanoparticles, respectively. (c) The schematic multiple scattering of light within the hierarchical ZnO photoelectrode composed by self-assembled ZnO secondary nanoparticles [46].

be particularly identified for 2 μm film. However, the absorption at wavelengths around 400–650 nm caused by the light scattering is enhanced dramatically with increasing the thickness of the ZnO photoelectrodes from 2 to 12μmm as shown in **Figure 16b**. Through a significant light scattering from the hierarchical structure, the thicker ZnO films provide the optical gallery that could provide more photon absorption in the visible region by the dye molecules.

The fabrication procedure of DSCs for ZnO NPs were similar to the ZnO NWs, but the photoelectrodes were prepared by screen-printing method. The molecular structures of the indoline-based organic dyes employed in this hierarchically packed ZnO photoelectrode are depicted in **Figure 17**. Both D149 and D205 sensitizers have double rhodanic acid as an anchor moiety. However, D205 is designed by introducing an octyl substitute into the terminal rhodanine ring to replace the ethyl group of D149 [51, 52]. In order to improve the DSCs performance, optimization of the thickness of the ZnO photoelectrode is necessary, because the photovoltaic characteristics exhibit significant variation depending on the thickness. **Figure 18a**, **b**

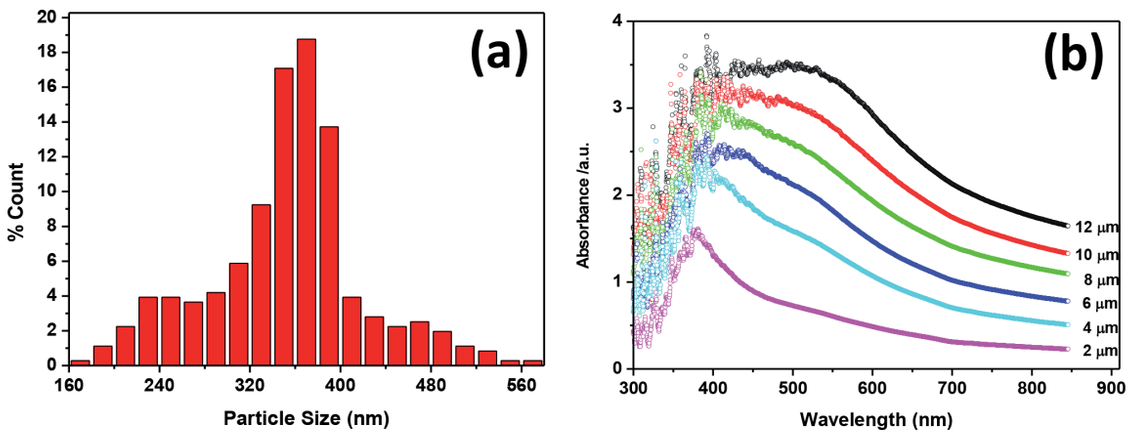

Figure 16.
(a) Diameter distribution for the ZnO secondary nanoparticles. (b) The corresponding optical absorption spectra of ZnO photoelectrodes with various film thicknesses, from 2 to 12 μm [50].

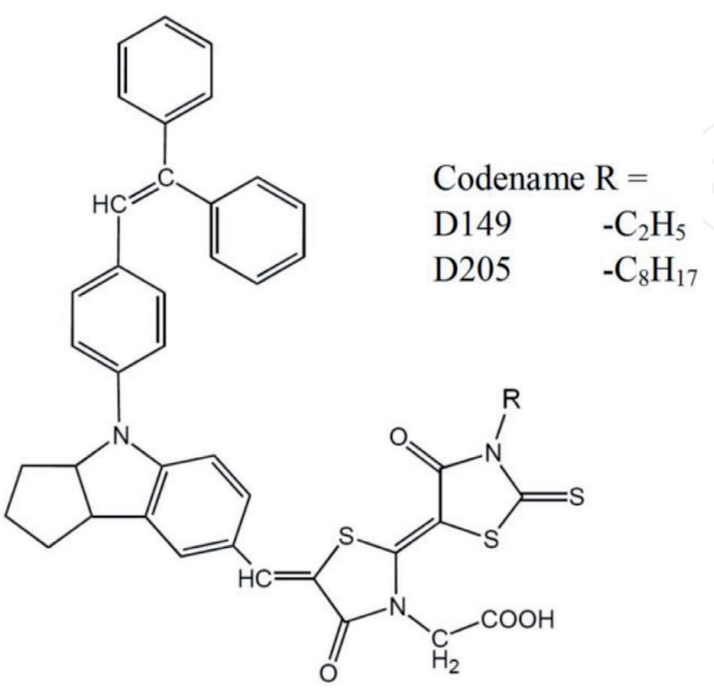

Figure 17.
Molecular structures of indoline D149 and D205 dyes.

compares the IPCE spectra of ZnO DSCs constructed using two indoline dyes with different film thicknesses. For both two indoline DSCs, IPCE increases significantly with thicker photoelectrodes but saturated at the thickness above 30 μm due to the limitation of electron diffusion length. The spectra at wavelengths shorter than 400 nm are deteriorated due to the UV cutoff effect caused by the thick glass substrate. The photocurrent peak at approximately 367 nm belongs to direct light harvesting of ZnO semiconductor, which remains almost unchanged due to the short penetration depth of UV light. **Figure 18a**, **b** also shows the maximal IPCE value increase gradually with the thickness of ZnO photoelectrode from 71 to 74% and 77 to 79% at wavelength of 550 nm for D149- and D205-sensitized DSCs, respectively. The optimal IPCE obtained for the D205-sensitized ZnO DSCs are

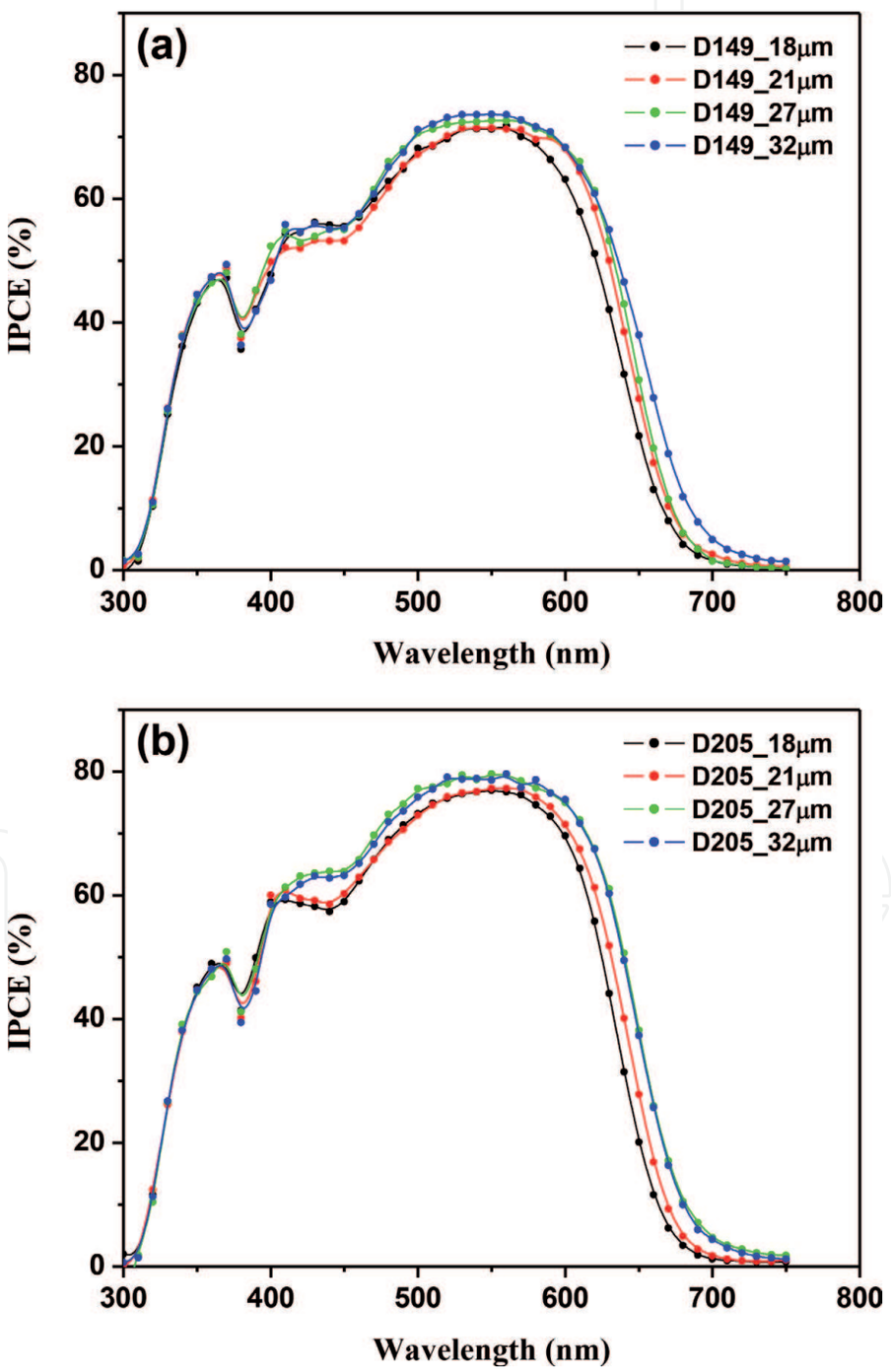

Figure 18.
Photocurrent action spectra of ZnO DSCs constructed using (a) D149 and (b) D205, with different photoelectrode thicknesses [50].

higher than the D149-sensitized DSCs in the visible-wavelength (400–700 nm) region. The numerous cracks in thick photoelectrode films (>32 μm) were also observed due to unpracticed-printing technique.

The comparison of photocurrent-voltage (J-V) of DSCs using 27-μm-thick ZnO photoelectrodes and two indoline dyes under AM 1.5 full sunlight illumination (100 mW cm^{-2}) and in the dark was shown in **Figure 19a**. For D205 uptake, the J-V plot reveals J_{sc} = 12.17 mA cm^{-2}, V_{oc} = 0.65 V, *FF* = 0.67, and η = 5.34%. The J-V plot of D149 uptake reveals J_{sc} = 10.94 mA cm^{-2}, V_{oc} = 0.64 V, *FF* = 0.71, and η = 4.95%. Both V_{oc} and J_{sc} for D205-sensitized ZnO DSCs are higher than D149-sensitized ones. As a result of the higher IPCE, the J_{sc} for the D205-sensitized ZnO DSCs is higher than the D149-sensitized ZnO ones. The dark current indicates that D205-sensitized ZnO DSCs have a slightly more negative-onset potential for the reduction of I_3^- than

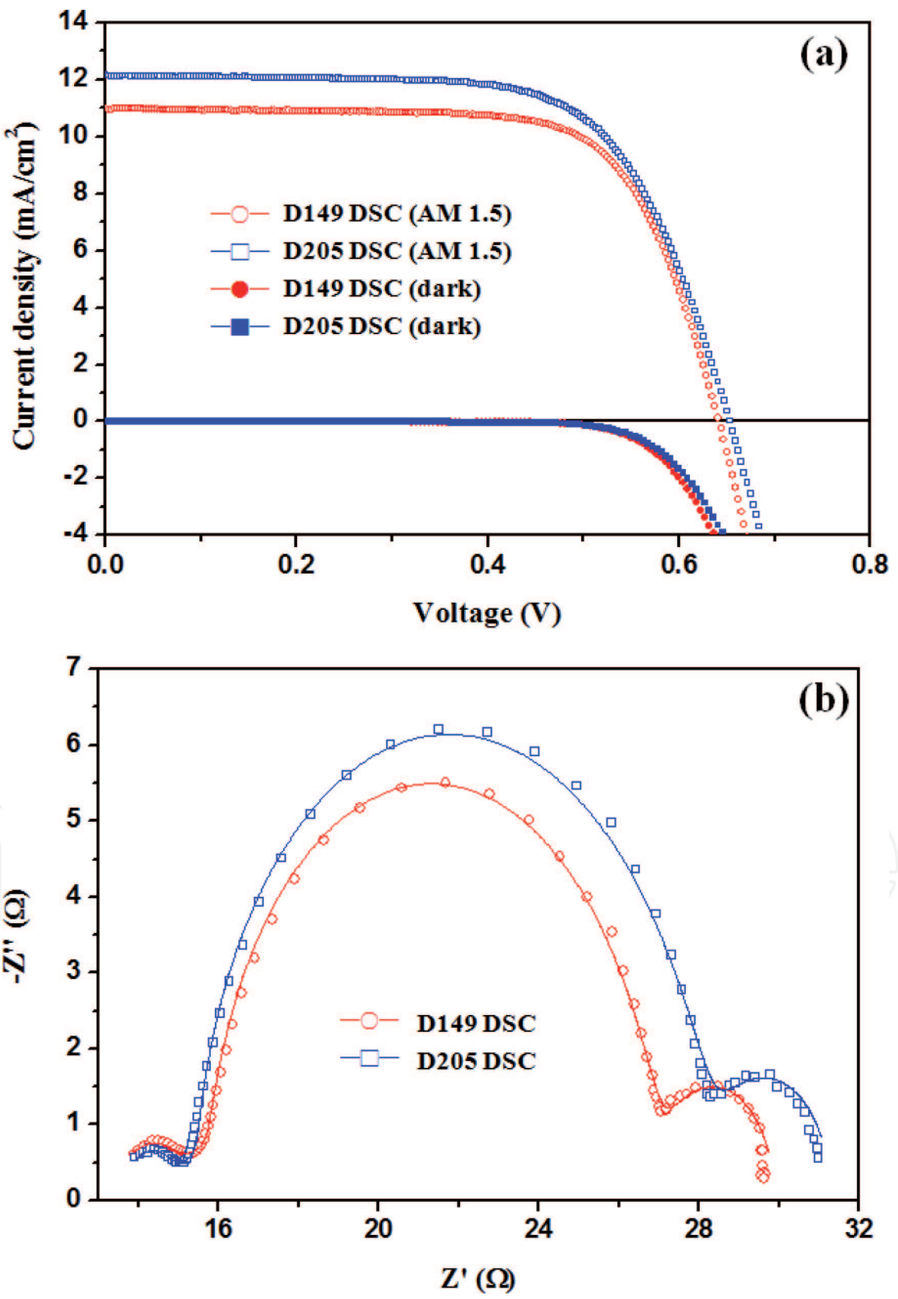

Figure 19.
Photovoltaic characteristics of DSCs with 27-μm-thick ZnO photoelectrodes and two different indoline dyes. (a) J-V curves for D149- and D205-sensitized DSCs with AM 1.5 illumination and in the dark, respectively. (b) Nyquist plots of D149- and D205-sensitized DSCs performed under illumination at the applied bias of V_{oc}. The solid lines are the fitting results [50].

D149-sensitized ZnO DSCs and could also be rationalized as a negative shift in edge of ZnO conduction band caused by D205 dye adsorption. The alkyl chain of the terminal rhodanine moiety of D205 has been extended from ethyl to octyl, which cause the effective suppression of electron recombination between I_3^- and efficient electrons injection into the photoelectrodes [53]. The dyes with the hydrophobic alkyl chains principally not only could form a barrier layer on the sensitizer dye to protect the dye layer against water intrusion from the electrolyte but also rearrange dyes that are more perpendicular to the ZnO surface.

As shown in **Figure 19b**, the obvious middle semicircle of the Nyquist plots belongs to the electron recombination resistance which means a superior circuit in D205-sensitized ZnO DSCs than that of D149-sensitized ZnO DSC. Like **Figure 12**, some interior parameters of the devices can be further derived by well-fitting the impedance data based on the modified equivalent circuit of DSCs as shown in **Figure 20**. The detail parameters are listed in **Table 3**. The electron loss rate k_{eff} in the D205-sensitized ZnO DSCs is smaller than the D149-sensitized ones, which causes the prolonged electron lifetime τ_{eff} in the D205-sensitized ZnO DSCs. The larger charge-transfer resistance R_k value for D205-sensitized ZnO DSCs indicates the less interfacial recombination occurring between the injected electrons of ZnO and the I_3^- of electrolyte. Moreover, the effective electron diffusion coefficient D_{eff} is also enhanced with utilization of D205 sensitizer. It is reasonable that the photocurrent density may be directly affected by changes in the electron recombination rate. The amphiphilic D205 may help the formation of a self-assembled dye monolayer that prevents photoelectrons from being resorbed by triiodide ions in the electrolyte, resulting in a higher V_{oc} and J_{sc} [54].

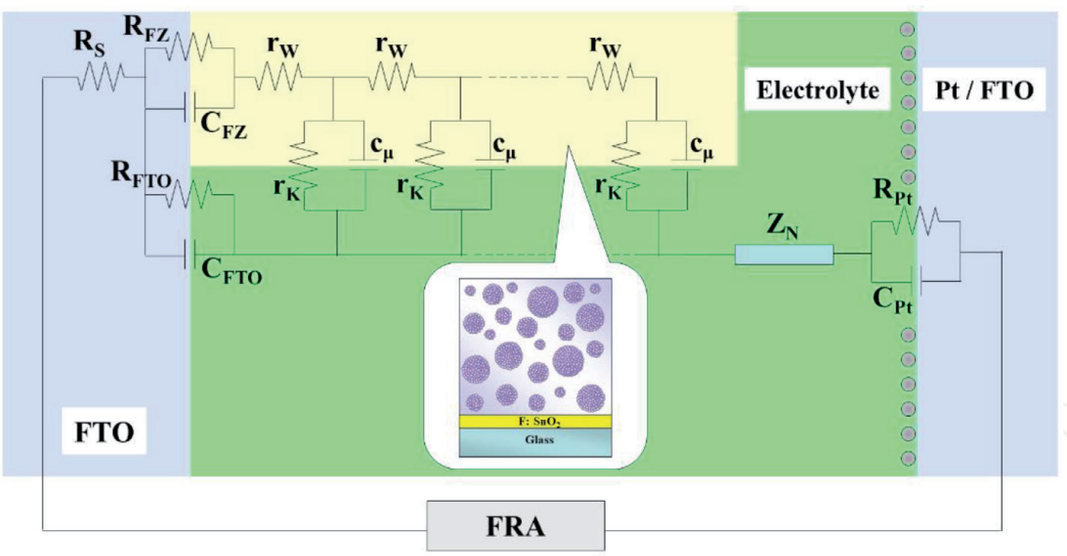

Figure 20.
The equivalent circuit model of ZnO DSCs composed with hierarchical nanoparticles [50].

ZnO DSCs	J_{sc} (mA/cm^2)	V_{oc} (V)	*FF*	η (%)	k_{eff} (s^{-1})	τ_{eff} (ms)	R_k (Ω)	R_w (Ω)	D_{eff} (cm^2/s)
D149	10.94	0.641	0.71	4.95	57.85	17.29	12.55	2.47	2.14×10^{-3}
D205	12.17	0.653	0.67	5.34	47.12	21.22	14.43	1.98	2.51×10^{-3}

Table 3.
Performances and electron transport properties of the D149- and D205-sensitized DSCs (27-μm-thick ZnO photoelectrode) determined by J-V characteristics and EIS analysis [50].

4. Conclusion

Low-dimensional NPs, QDs, and NWs have attracted considerable attention owing to their interesting physical and chemical properties. ZnO NWs can shed the light to conduct electronic, optoelectronic, electrochemical, and electromechanical devices with nanoscale dimensions because of the excellent electrical transport and photonic interconnection due to their crystallinity. ZnO QDs and NPs are of great interest because of the three-dimensional confinement of carrier, and phonon leads not only continuous tuning of the optoelectronic properties but also improvement in device performance. As a wide-bandgap semiconductor, ZnO has been reported as an alternative for DSCs because ZnO offers a large direct bandgap which is similar to TiO_2 and even higher electron mobility. ZnO also can be tailored to various nanostructures that provides a promising means for improving the performance of the photoelectrode in DSCs. It is of great urgency to effectively design and control the process window that enables the seamless integration not only the mass production but reproducibility of ZnO nanostructures for the near future.

Author details

Hsin-Ming Cheng* and Shun-Wei Liu*
Department of Electronic Engineering and Organic Electronics Research Center, Ming Chi University of Technology, New Taipei City, Taiwan

*Address all correspondence to: smcheng@mail.mcut.edu.tw and swliu@mail.mcut.edu.tw

References

[1] Kaidashev EM, Lorenz M, von Wenckstern H, Rahm A, Semmelhack HC, Han KH, et al. High electron mobility of epitaxial ZnO thin films on c-plane sapphire grown by multistep pulsed-laser deposition. Applied Physics Letters. 2003;**82**:3901

[2] Law M, Greene LE, Johnson JC, Saykally R, Yang P. Nanowire dye-sensitized solar cell. Nature Materials. 2005;**4**:455

[3] Baxter JB, Aydil ES. Nanowire-based dye-sensitized solar cells. Applied Physics Letters. 2005;**86**:053114

[4] Cheng HM, Chiu WH, Lee CH, Tsai SY, Hsieh WF. Formation of Branched ZnO Nanowires from Solvothermal Method and Dye-Sensitized Solar Cells Applications. The Journal of Physical Chemistry C. 2008;**112**(42):16359

[5] Wang ZL, Kong XY, Zuo JM. Induced Growth of Asymmetric Nanocantilever Arrays on Polar Surfaces. Physical Review Letters. 2003;**91**:185502

[6] Yan H, He R, Johnson J, Law M, Saykally R, Yang P. Dendritic Nanowire Ultraviolet Laser Array. The Journal of the American Chemical Society. 2003;**125**:4728

[7] Cheng HM, Hsu HC, Chen SL, Wu WT, Kao CC, Lin LJ, et al. Efficient UV photoluminescence from monodispersed secondary ZnO colloidal spheres synthesized by sol-gel method. Journal of Crystal Growth. 2005;**277**:192

[8] Seelig EW, Tang B, Yamilov A, Cao H, RPH C. Self-assembled 3D photonic crystals from ZnO colloidal spheres. Materials Chemistry and Physics. 2003;**80**:257

[9] Ocaña M, Clemente R, Serna CJ. Uniform colloidal particles in solution: Formation mechanisms. Journal of Advanced Materials. 1995;**7**:212

[10] Cheng HM, Lin KF, Hsu HC, Lin CJ, Lin LJ, Hsieh WF. Enhanced Resonant Raman Scattering and Electron–Phonon Coupling from Self-Assembled Secondary ZnO Nanoparticles. The Journal of Physical Chemistry B. 2005;**109**(39):18385

[11] Murray CB, Kagan CR, Bawendi MG. Self-Organization of CdSe Nanocrystallites into Three-Dimensional Quantum Dot Superlattices. Science. 1995;**270**:1335

[12] Murray CB, Sun SH, Gaschler W, Doyle H, Betley TA, Kagan CR. Colloidal synthesis of nanocrystals and nanocrystal superlattices. The IBM Journal of Research and Development. 2001;**45**(1):47

[13] Parke G, Shindo D, Waseda Y, Sugimoto TJ. Internal Structure Analysis of Monodispersed Pseudocubic Hematite Particles by Electron Microscopy. The Journal of Colloid and Interface Science. 1996;**177**:198

[14] Sugimoto T, Wang Y, Itoh H, Muramatsu A. Systematic control of size, shape and internal structure of monodisperse α-Fe2O3 particles. Colloids and Surfaces A: Physicochemical and Engineering Aspects. 1998;**134**:265

[15] Sugimoto T, Sakata K, Muramatsu A. Formation Mechanism of Monodisperse Pseudocubic α-Fe_2O_3 Particles from Condensed Ferric Hydroxide Gel. The Journal of Colloid and Interface Science. 1993;**159**:372

[16] Sugimoto T, Khan MM, Muramatsu A. Formation mechanism of monodisperse peanut-type α-Fe_2O_3 particles from condensed ferric

hydroxide gel. Colloids and Surfaces A: Physicochemical and Engineering Aspects. 1993;**79**:233

[17] Sugimoto T, Muramatsu A, Sakata K, Shindo DJ. Characterization of hematite particles of different shapes. The Journal of Colloid and Interface Science. 1993;**158**:420

[18] Exarhos GJ, Sharma SK. Influence of processing variables on the structure and properties of ZnO films. Thin Solid Films. 1995;**270**:27

[19] Xu XL, Lau SP, Chen JS, Che GY, Tay BKJ. Polycrystalline ZnO thin films on Si (100) deposited by filtered cathodic vacuum arc. Journal of Crystal Growth. 2001;**223**:201

[20] Ashkenov N, Mbenkum BN, Bundesmann C, Riede V, Lorenz M, Spemann D, et al. Infrared dielectric functions and phonon modes of high-quality ZnO films. Journal of Applied Physics. 2003;**93**:126

[21] Damen TC, Porto SPS, Tell B. Raman Effect in Zinc Oxide. Physics Review. 1966;**142**:570

[22] Scott JF. UV Resonant Raman Scattering in ZnO. Physical Review B. 1970;**2**:1209

[23] Zhang XT, Liu YC, Zhi ZZ, Zhang JY, Lu YM, Shen DZ, et al. Resonant Raman scattering and photoluminescence from high-quality nanocrystalline ZnO thin films prepared by thermal oxidation of ZnS thin films. Journal of Physics D. 2001;**34**(24):3430

[24] Ursaki VV, Tiginyanu IM, Zalamai VV, Masalov VM, Samarov EN, Emelchenko GA, et al. Photoluminescence and resonant Raman scattering from ZnO-opal structures. Journal of Applied Physics. 2004;**96**:1001

[25] Ng HT, Chen B, Li J, Han J, Meyyappan M, Wu J, et al. Optical properties of single-crystalline ZnO nanowires on *m*-sapphire. Applied Physics Letters. 2003;**82**:2023

[26] Cheng HM, Hsu HC, Tseng YK, Lin LJ, Hsieh WF. Raman Scattering and Efficient UV Photoluminescence from Well-Aligned ZnO Nanowires Epitaxially Grown on GaN Buffer Layer. The Journal of Physical Chemistry. B. 2005;**109**:8749

[27] Alivisatos AP, Harris TD, Carroll PJ, Steigerwald ML, Brus LE. Electron–vibration coupling in semiconductor clusters studied by resonance Raman spectroscopy. The Journal of Chemical Physics. 1989;**90**:3463

[28] Klein MC, Hache F, Ricard D, Flyzanis C. Size dependence of electron-phonon coupling in semiconductor nanospheres: The case of CdSe. Physical Review B. 1990;**42**:11123

[29] Callender RH, Sussman SS, Selders M, Chang RK. Dispersion of Raman Cross Section in CdS and ZnO over a Wide Energy Range. Physical Review B. 1973;**7**:3788

[30] Alim KA, Fonoberov VA, Balandin AA. Origin of the optical phonon frequency shifts in ZnO quantum dots. Applied Physics Letters. 2005;**86**:053103

[31] Alim KA, Fonoberov VA, Shamsa M, Balandin AA. Micro-Raman investigation of optical phonons in ZnO nanocrystals. Journal of Applied Physics. 2005;**97**:124313

[32] Bartolo BD, Powell R. Phonons and Resonances in Solids. New York: Wiley; 1976. Chap. 10

[33] Böer KW. Survey of Semiconductor Physics. New York: Van Nostrand Reinhold; 1990. Chap. 20

[34] Scamarcio G, Spagnolo V, Ventruti G, Lugara M, Righini GC. Size

dependence of electron—LO-phonon coupling in semiconductor nanocrystals. Physical Review B. 1996;**53**:R10489

[35] Kaminow IP, Johnston WD. Quantitative Determination of Sources of the Electro-Optic Effect in $LiNbO_3$ and $LiTaO_3$. Physics Review. 1967;**160**:519

[36] Loudon R. The Raman effect in crystals. Advances in Physics. 1964;**13**(52):423

[37] Makino T, Tamura K, Chia CH, Segawa Y, Kawasaki M, Ohtomo A, et al. Size dependence of exciton–longitudinal-optical-phonon coupling in ZnO/Mg0.27Zn0.73O quantum wells. Physical Review B. 2002;**66**:233305

[38] Wang RP, Xu G, Jin P. Size dependence of electron-phonon coupling in ZnO nanowires. Physical Review B. 2004;**69**:113303

[39] Wu JJ, Wang DKP. Fabrication and Impedance Analysis of n-ZnO Nanorod/p-Si Heterojunctions to Investigate Carrier Concentrations in Zn/O Source- Ratio-Tuned ZnO Nanorod Arrays. Advanced Materials. 2015;**2007**:19

[40] Wu JJ, Chen GR, Yang HH, Ku CH, Lai JY. Effects of dye adsorption on the electron transport properties in ZnO-nanowire dye-sensitized solar cells. Applied Physics Letters. 2007;**90**:213109

[41] Wang Q, Ito S, Grätzel M, Fabregat-Santiago F, Mora-Seró I, Bisquert J, et al. Characteristics of High Efficiency Dye-Sensitized Solar Cells. The Journal of Physical Chemistry. B. 2006;**110**:25210

[42] Mora-Seró I, Bisquert J, Fabregat-Santiago F, Garcia-Belmonte G, Zoppi G, Durose K, et al. Implications of the Negative Capacitance Observed at Forward Bias in Nanocomposite and Polycrystalline Solar Cells. Nano Letters. 2006;**6**:640

[43] Adachi M, Sakamoto M, Jiu J, Ogata Y, Isoda S. Determination of Parameters of Electron Transport in Dye-Sensitized Solar Cells Using Electrochemical Impedance Spectroscopy. The Journal of Physical Chemistry. B. 2006;**110**:13872

[44] Pasquier AD, Chen H, Lu Y. Dye sensitized solar cells using well-aligned zinc oxide nanotip arrays. Applied Physics Letters. 2006;**89**:253513

[45] Chou TP, Zhang Q, Cao G. Effects of Dye Loading Conditions on the Energy Conversion Efficiency of ZnO and TiO2 Dye-Sensitized Solar Cells. Journal of Physical Chemistry C. 2007;**111**:18804

[46] Cheng HM, Hsieh WF. High-efficiency metal-free organic-dye-sensitized solar cells with hierarchical ZnO photoelectrode. Energy and Environmental Science. 2010;**3**(4):442

[47] Cao H, Zhao YG, Ho ST, Seelig EW, Wang QH, Chang RPH. Random Laser Action in Semiconductor Powder. Physical Review Letters. 1999;**82**:2278

[48] Chou TP, Zhang Q, Fryxell GE, Cao G. Hierarchically Structured ZnO Film for Dye-Sensitized Solar Cells with Enhanced Energy Conversion Efficiency. Advanced Materials. 2007;**19**:2588

[49] Zhang Q, Chou TP, Russo B, Jenekhe SA, Cao G. Aggregation of ZnO nanocrystallites for high conversion efficiency in dye-sensitized solar cells. Angewandte Chemie International Edition. 2008;**47**:2402

[50] Cheng HM, Hsieh WF. Electron transfer properties of organic dye-sensitized solar cells based on indoline sensitizers with ZnO nanoparticles. Nanotechnology. 2010;**21**(48):485202

[51] Ito S, Miura H, Uchida S, Takata M, Sumioka K, Liska P, et al. High-conversion-efficiency

organic dye-sensitized solar cells with a novel indoline dye. Chemical Communications. 2008:5194

[52] Kuang D, Uchida S, Humphry-Baker R, Zakeeruddin SM, Grätzel M. Organic dye-sensitized ionic liquid based solar cells: remarkable enhancement in performance through molecular design of indoline sensitizers. Angewandte Chemie, International Edition. 2008;**47**:1923

[53] Kroeze JE, Hirata N, Koops S, Nazeeruddin MK, Schmidt-Mende L, Grätzel M, et al. Alkyl Chain Barriers for Kinetic Optimization in Dye-Sensitized Solar Cells. Journal of the American Chemical Society. 2006;**128**:16376

[54] Horiuchi T, Miura H, Uchida S. Highly-efficient metal-free organic dyes for dye-sensitized solar cells. Chemical Communications. 2003:3036